View metadata, citation and similar papers at core.ac.uk

brought to you by CORE

provided by Caltech Authors

www.sciencemag.org/cgi/content/full/science.aad3749/DC1

Supplementary Materials for

Ultrahigh power factor and thermoelectric performance in hole-doped single-crystal SnSe

Li-Dong Zhao,* Gangjian Tan, Shiqiang Hao, Jiaqing He, Yanling Pei, Hang Chi, Heng Wang, Shengkai Gong, Huibin Xu, Vinayak P. Dravid, Ctirad Uher, G. Jeffrey Snyder, Chris Wolverton, Mercouri G. Kanatzidis*

*Corresponding author. E-mail**:** zhaolidong@buaa.edu.cn (L.-D.Z.); m-kanatzidis@northwestern.edu (M.G.K.)

Published 26 November 2015 on *Science* Express
DOI: 10.1126/science.aad3749

This PDF file includes:

Supplementary Materials outline

1. Materials and Methods

Starting materials: Sn chunk (99.999%, American Elements, US), Se shot (99.999%, 5N Plus, Canada) and Na chunk (99.999%, Aldrich, U.S.).

Bridgman crystal growth: The synthesis of single crystal SnSe can be challenging. A typical process used in our laboratory is given below. Ingots (~20 g) with nominal compositions of hole doped SnSe were synthesized by mixing appreciated ratios of high purity starting materials of Sn, Se and Na in carbon-coated fused silica tubes. The tubes were evacuated to a pressure of ~10^{-4} torr, flame-sealed, slowly heated to 1223 K in 10 h, soaked at this temperature for 6 h and subsequently furnace cooling to room temperature. The obtained ingots were crushed into powders and charged into a conical carbon-coated silica tube, evacuated and flame-sealed. Then the conical silica tube was placed inside another bigger fused silica tube, which was then evacuated and flame-sealed. The outer tube is used to prevent the crystal from oxidation by air because the inner tube can often break owing to the high temperature phase transition and considerable difference of thermal expansion between the crystal and silica. This is why thick wall tubes are recommended. The SnSe crystals with dimensions of 13 mm (diameter) × 20 mm (length) were obtained. The manipulations and preparative steps were carried out in a purified N_2-atmosphere glove box with total O_2 and H_2O level < 0.1 ppm.

Electrical transport properties: The obtained hole doped SnSe crystals were cut into bars along different directions with dimensions 10 mm × 2.5 mm × 2.5 mm, which were used for simultaneous measurement of the Seebeck coefficient and the electrical conductivity using an UlvacRiko ZEM-3 instrument under a helium atmosphere from room temperature to 773 K. The samples were coated with a thin (~0.1-0.2 mm) layer of boron nitride (BN) to protect instruments, the manipulations and preparative steps can be referenced as explained in detail previously (*29*).

Hall and low-temperature transport property measurements: The Hall measurement was performed on homemade apparatuses (University of Michigan). The low temperature Hall coefficients were carried out in the temperature range of 10-300 K on samples with dimensions 6 mm × 2 mm × 1 mm in a cryostat equipped with a radiation shield using a Linear Research ac bridge with 16 Hz excitation in a magnet cryostat capable of fields up to 5 T. High temperature Hall coefficients were measured with a homemade high temperature apparatus, which provides a working range from 300-773 K. The sample with dimensions 8 mm × 3 mm × 1 mm was mounted and protected with argon gas atmosphere to avoid possible oxidation at high

temperature. The Hall resistance was monitored with a Linear Research AC Resistance Bridge (LR-700), with constant magnetic fields of ± 1 T applied by using an Oxford Superconducting Magnet. Low temperature transport property measurements were carried out over the temperature range of 10-300 K. Electrical conductivity and Seebeck coefficient were determined using a longitudinal steady-state technique in a homemade cryostat. The uncertainties of electrical conductivity and Seebeck coefficient are estimated to be ± 3% and ± 3%, respectively. Hall coefficients and electrical transport properties as a function of temperature for hole doped SnSe crystal are shown in Fig. S3.

Thermal conductivity: The hole doped SnSe crystals were cut and polished into rectangular sample with side length of 6 mm and ~ 2 mm thickness for thermal diffusivity measurements along different directions. The samples were coated with a thin layer of graphite to minimize errors from the emissivity of the material. The thermal conductivity was calculated from $\kappa=D\cdot C_p\cdot\rho$, where the thermal diffusivity coefficient (D) was measured along the same direction as the electrical transport using the laser flash diffusivity method in a Netzsch LFA457 (Northwestern University), the thermal diffusivity coefficient (D) was reconfirmed using the laser flash diffusivity method in a Netzsch LFA427 (Beihang University) and a Netzsch LFA457 (California Institute of Technology), respectively; the specific heat capacity (C_p) was indirectly derived using a representative sample (Pyroceram 9606) in the range from 300-773K, the C_p results show good agreement with the reported values (*18*, *36*); and the density (ρ) was determined using the dimensions and mass of the sample and then reconfirmed using a gas pycnometer (Micromeritics AccuPyc1340) measurements. Density values between 5.8-6.1 g/cm^3 were measured. The thermal diffusivity data were analyzed using a Cowan model with pulse correction and heating and cooling cycles give reproducible values for each sample.

The heat capacity (C_p) and thermal diffusivity (D) dependence of temperature are shown in Figs. S2A and 2B, the C_p values of SnSe from other reports are also plotted for comparison (*18*, *36*). The total thermal conductivity (κ_{tot}) is the sum of the electronic (κ_{ele}) and lattice thermal conductivity (κ_{lat}). κ_{ele} is proportional to the electrical conductivity (σ) through the Wiedemann-Franz relation (*24*), $\kappa_{ele} = L\sigma T$, where L is the Lorenz number. Due to the complexity and the non-parabolicity of the valence band structure around the Fermi level for hole doped SnSe, a more accurate determination of L based on multi band model is determined, Fig. S2C.

Thermogravimetric analysis (TGA) measurements: The thermogravimetric analysis (TGA) measurements were performed on a Shimadzu TGA-50 thermogravimetric analyzer in aluminum boats under a N_2 flow and air, in the temperature range from 300-873 K with a rate of 5 K min^{-1}.

***ZT* measurement uncertainty:** The measurement of σ, S and κ (from the sample density ρ, heat capacity C_p, and thermal diffusivity D), each has an uncertainty of 3 % to 20 %. The uncertainty in *ZT* could easily reach a large measurement uncertainty as follows.

$$\frac{\Delta Z}{Z} = 2\frac{\Delta S}{S} + \frac{\Delta \sigma}{\sigma} + \frac{\Delta \rho}{\rho} + \frac{\Delta C_p}{C_p} + \frac{\Delta D}{D} \qquad (1)$$

We carried out heating and cooling cycles for the multiple measurements along different crystallographic directions. We found good repeatability for the electrical transport properties, the uncertainty of the electrical conductivity is 5 % and Seebeck coefficient measurements is 3 %, see Figs. S(5-8)A and S(5-8)B. Combining the uncertainties of electrical conductivity and Seebeck coefficient, the measurement uncertainty is about 11 % for the power factor, see Figs. S(5-8)C. The uncertainty for the total thermal conductivity is about 12 % (comprising uncertainties of 5 % for the thermal diffusivity, 5 % for the specific heat, and 2 % for the density), see Figs. S(5-8)D. The combined uncertainty for all measurements involved in the calculation of *ZT* is around 20 %, see Figs. S(5-8)E. To exclude the effects of composition stoichiometric ratio of SnSe on the final *ZT* as suggested by Serrano-Sanchez *et al* (*26*), we carried out the thermogravimetric analysis (TGA) measurements. The TGA results indicate that the hole doped SnSe single csytals are stable at the teperature up to 873K in both N_2 and air atmosphere, see Fig. S9, which is consistent with the TGA observations by Agarwal *et al* (*37*).

To validate the high thermoelectric performance of hole doped SnSe along *b* axis as best as we could, we measured the thermal conductivities at Northwestern University, Beihang University and California Institute of Technology, respectively. We found a spread in the thermal conductivities with an uncertainty of about 20 %, Fig. S10. When the power factor was fixed at the average value from Figs. S(5-8) C, the lower thermal conductivities will show higher *ZT*s. Figure S11 shows that the room temperature *ZT* ranges from 0.6 to 0.9 and the ZT_{max} ranges from 1.6 to 2.4. To be conservative in the main text we show the average ZT_{max} ranging from 0.7 to 2.0 from 300-773K.

Transmission electron microscopy (TEM): The TEM specimens were prepared by conventional standard methods, that is, cutting, grinding, dimpling, polishing and Ar-ion milling with a liquid nitrogen cooling stage. The hole doped SnSe tend to be quite moisture sensitive, therefore all procedures are done by the use of a water-free liquid. S/TEM investigations were carried out in JEOL 2100F and double Cs corrected ARM200F microscopes. Figure S12 shows the low-magnification image of the typical regions of the hole doped SnSe in TEM model and STEM model.

Density functional theory (DFT) calculations: The total energies and relaxed geometries were calculated by DFT within the generalized gradient approximation of Perdew-Burke-Ernzerhof to the exchange correlation functional with Projector Augmented Wave potentials (*38, 39*). We use periodic boundary conditions and plane wave basis sets as implemented in the Vienna *ab initio* simulation package (*40*). The total energies were numerically converged to approximately 3meV/cation with spin-orbit coupling using a basis set energy cutoff of 500 eV and dense *k*-meshes corresponding to 3000 *k*-points per reciprocal atom in the Brillouin zone. The low-temperature crystal structure of SnSe has a *Pnma* space group in the temperature range of 300-790 K, with experimental lattice parameters a = 11.58 Å, b = 4.22 Å, and c = 4.40 Å. Our DFT-relaxed *Pnma* SnSe lattice constants are a = 11.794 Å, b = 4.215 Å, and c = 4.550 Å, which are in reasonably good agreement with the experimental values.

From the DFT band structure of the *Pnma* phase as shown in Fig.3C, the first valence band maximum (VBM) is at (0.0, 0.0, 0.35) along the *Γ*-*Z* direction of the first Brillouin zone. There is also a local valence-band maximum at (0.0, 0.0, 0.44) that lies 0.06 eV lower in energy than the first VBM. For these two maxima, the effective masses are calculated by fitting the *E*-*k* bands around the VBM for the different directions, where the effective mass m^* is defined as:

$$m^* = \hbar^2 \left(\frac{\partial^2 E}{\partial k^2} \right)^{-1} \qquad (2)$$

where $\hbar$ is the reduced Planck constant.

In a multiband system where more than one band contributes to the thermoelectric performance the following expression may be used to define the key materials parameters that contribute to *ZT* (*19, 24, 41, 42*):

$$ZT_{\max} \propto \frac{T^{5/2}}{\kappa_{lat}} \exp\left(r + \frac{1}{2}\right)\left[\gamma_1\tau_1\sqrt{\frac{m_{x_1}\cdot m_{y_1}}{m_{z_1}}} + \gamma_2\tau_2\sqrt{\frac{m_{x_2}\cdot m_{y_2}}{m_{z_2}}} + \cdots\right] \qquad (3)$$

where γ_1, γ_2 *etc* is the degeneracy of band extrema in the Brillouin zone for band 1, 2 *etc*, m_i is the effective mass of the carriers (electrons or holes) in the i^{th} crystal direction, τ_1, τ_2 is the relaxation time of the carriers moving along the transport (z) direction for each band, r is the scattering parameter, and κ_{lat} is the lattice thermal conductivity. The degeneracy of band extrema (γ) in the Brillouin zone is the number of valleys in the conduction band (relevant to *n*-type materials) or peaks in the valence band (relevant to *p*-type materials). In the orthorhombic crystal symmetry of SnSe $\gamma = 2$. In SnSe the presence of more than one types of band (each band with a $\gamma = 2$) near the Fermi level leads to increased *ZT* because the total power factor for the material derives from the summation of contributions from all relevant bands.

In addition to γ, Eq. (3) also implies that high effective mass anisotropy i.e. high ($m_x m_y/m_z$) ratio is critical to high *ZT*. If transport is taken to be along the *z*-direction of the crystal, a small effective mass (m_z) along this direction coupled with large masses along the *x*- and *y*-directions (m_x and m_y) is important. Taking the effective mass parameters m_x, m_y, m_z, from the DFT calculations we can assess the fractions ($m_x m_y/m_z$) for each band for each crystal direction. The high anisotropy in the crystal structure of SnSe (Fig. 4) gives rise to sqrt ($m_x m_y/m_z$) ratios highest along the *c*- and *b*-directions (for all relevant valence bands). For example, for the first band (Γ-*Z*) sqrt ($m_x \cdot m_y/m_z$) = 1.34 sqrt (m_0) along the *c*- direction, 0.56 sqrt (m_0) for the *b*- direction, and 0.25 sqrt (m_0) for the *a*- direction, where m_0 is the free electron mass. For the 2nd band (Γ-*Y*) sqrt ($m_x \cdot m_y/m_z$) = 1.62 sqrt (m_0) for the *c*- direction, 1.72 sqrt (m_0) *b*- direction, and 0.11 sqrt (m_0) for the *a*- direction. This is consistent with the experimental fact that the *b*- and *c*-axes of the crystal are the high performance directions.

Boltzmann transport calculations: We have used Boltzmann theory to compute semi-classical values of the Seebeck coefficient and electrical conductivity from the DFT-computed electronic structure. We used the program Boltztrap for these calculations (*43*). In these calculations, the electrical conductivity and Seebeck coefficient tensor are all integrated over all electronic states. In the framework of semiclassical transport theory, a useful way of describing the collisional term in the Boltzmann equation is to define a relaxation-time $\tau_{n,k}$ for an electron in a band *n* at wave vector *k*. Then, we obtain the following expressions for the transport tensors as

a function of the electron chemical potential μ (that depends on the doping level of the system in a semiconductor) and of the temperature *T*.

$$\sigma_{ij}(T,\mu) = e^2 \int -\frac{\partial f_\mu(T,\varepsilon)}{\partial \varepsilon} \sigma_{ij}(\varepsilon) d\varepsilon \qquad (4)$$

$$(\sigma S)_{ij}(T,\mu) = \frac{e}{T} \int \left(-\frac{\partial f_\mu(T,\varepsilon)}{\partial \varepsilon} \right) (\varepsilon - \mu) \sigma_{ij}(\varepsilon) d\varepsilon \qquad (5)$$

Here σS denotes the matrix product of the two tensors, and $\partial f_\mu / \partial \varepsilon$ is the derivative of the Fermi-Dirac distribution function with respect to the energy. Moreover, we have defined the above quantities in terms of the transport distribution function $\sigma_{ij}(\varepsilon)$, defined as:

$$\sigma_{ij}(\varepsilon) = \frac{1}{V} \sum_{n,k} \upsilon_i(n,k) \upsilon_j(n,k) \tau_{n,k} \delta(\varepsilon - \varepsilon_{n,k}) d\varepsilon \qquad (6)$$

where the summation is over all bands, *n*, and over all the Brillouin zone wave vectors, *k*. $\varepsilon_{n,k}$ is the energy for band *n* at *k* and $\upsilon_i(n,k)$ is the *i*-th component of the band velocity at (n,k) as given by

$$\upsilon_i(n,k) = \frac{2\pi}{h} \frac{\partial \varepsilon_{n,k}}{\partial k_i} \qquad (7)$$

Our calculations show that the Seebeck coefficient decreases with increasing carrier concentration, see Fig. S13. We assume that the low concentration case is related to a single band and multiband contributions become more prominent for higher hole concentrations. As carrier concentration *n* increases, our calculated Seebeck coefficients decrease significantly more slowly than the $n^{-2/3}$ dependence expected from a single parabolic band, indicating when the doping becomes sufficient to bring multiple bands into play. At 750K, as the hole concentration increases by a factor of 3 (from 2×19 cm^{-3} to 6×19 cm^{-3}), a single band model would predict a decrease in the Seebeck coefficient from +380 μVK^{-1} to +190 μVK^{-1}. Our multiband calculations in the figure below show a decrease from + 380 μVK^{-1} to only +290 μVK^{-1}, hence a Seebeck coefficient significantly larger than this single band model.

We also investigated the Seebeck coefficients as a function of carrier concentration at 300 K to explore the multiband effects. As shown in main text Fig. 3B, the Seebeck coefficients depicted by the red circles are calculated by the Boltztrap code, which include full bands as

shown in the band structure of Fig. 3C. The blue squares are calculated by the single band model of the so-called Pisarenko formula:

$$S = \frac{k_B}{e}\left[\frac{2F_1(\eta)}{F_0(\eta)} - \eta\right] \qquad (8)$$

where Fermi integral is

$$F_x(\eta) = \int_0^\infty \frac{\varepsilon^x}{1 + \exp(\varepsilon - \eta)} d\varepsilon \qquad (9)$$

and reduced Fermi level η is determined by carrier concentration,

$$n = \frac{(2m_d^* k_B T)^{3/2}}{2\pi^2 \hbar^3} \frac{F_{1/2}(\eta)}{r_H} \qquad (10)$$

where Hall radius is

$$r_H = \frac{3}{4} \frac{F_{1/2}(\eta) F_{-1/2}(\eta)}{[F_0(\eta)]^2} \qquad (11)$$

m_d^* is the density of state (DOS) effective mass, p the hole density, k_B the Boltzmann constant, $\hbar$ the reduced Planck's constant, e the electronic charge and T the temperature. Here the DOS effective mass can be expressed as $m_d^* = (m_{kx}^* m_{ky}^* m_{kz}^*)^{1/3} A^{2/3}$, where m_{kx}^*, m_{ky}^*, and m_{kz}^* are the calculated effective masses based on the first band of the valence band maximum (shown in Fig. 3C), which are respectively 0.74 m_0, 0.33 m_0 and 0.14 m_0, A is the degeneracy of hole pockets in Brillouin zone, which is 2 in our case. So the DOS effective mass is 0.47 m_0. As can be seen, all Seebeck coefficients calculated from the single band model are lower than the full Boltztrap multiband integration, even at very low carrier concentration, (e.g. at 1×10^{17} cm^{-3}). This difference indicates the large Seebeck coefficient in this system is a reflection of multiband effects, and is consistent with the very small energy difference between the valence band maximum (first band) and the second band, where the DFT calculated value is 0.06 eV and experimental value 0.02 eV.

Another more intuitive way to explain why heavily doped semiconductors with multiple band transport exhibit higher Seebeck coefficients than those with single band transport (with the same carrier density) is given by the well-known equation (for a parabolic bands) below (*11*):

$$S = \frac{8\pi^2 k_B^2 T}{3eh^2} m_d^* \left(\frac{\pi}{3n}\right)^{2/3} \qquad (12)$$

where k_B is the Boltzmann constant, e the electron charge, h the Planck constant, T the Kelvin temperature, m_d^* the density of states effective mass, and n the hole concentration. The density of states effective mass (m_d^*) resulting from multiple bands lying close in energy is higher than that from a single band. This results in an enhanced Seebeck coefficient (*12*, *31*, *44*, *45*).

Lorenz number calculations: The Lorenz number L_{tot} was calculated based on a multi band model (*46*, *47*):

$$L_{tot} = \frac{L_1\sigma_1 + L_2\sigma_2}{\sigma_1 + \sigma_2} \qquad (13)$$

Where $L_{1,2}$ and $\sigma_{1,2}$ are the Lorenz number and electrical conductivity of band 1 and band 2, respectively.

$$L_1 = \left(\frac{k_B}{e}\right)^2 \left\{ \frac{{}^2F_{-2}^{\,1}(\eta,\beta_1)}{{}^0F_{-2}^{\,1}(\eta,\beta_1)} - \left[\frac{{}^1F_{-2}^{\,1}(\eta,\beta_1)}{{}^0F_{-2}^{\,1}(\eta,\beta_1)}\right]^2 \right\} \qquad (14)$$

and

$$L_2 = \left(\frac{k_B}{e}\right)^2 \left\{ \frac{{}^2F_{-2}^{\,1}(\eta_2,\beta_2)}{{}^0F_{-2}^{\,1}(\eta_2,\beta_2)} - \frac{{}^1F_{-2}^{\,1}(\eta_2,\beta_2)}{{}^0F_{-2}^{\,1}(\eta_2,\beta_2)} \right\} \qquad (15)$$

$$\sigma_1 = en_1\mu_1, \sigma_2 = en_2\mu_2 \qquad (16)$$

The carrier concentration n_1, n_2 and mobility μ_1 and μ_2 for band 1 and band 2 are respectively calculated by following equations (*19*):

$$n_1 = \frac{1}{3\pi^2}\left(\frac{2m_1^* k_B T}{h^2}\right)^{3/2} {}^0F_0^{\,3/2}(\eta,\beta_1) \qquad (17)$$

$$\mu_1 = \frac{2\pi h^4 eC_l}{m_l^*\left(2m_d^* k_B T\right)^{3/2} E_{def}^2} \frac{3\,{}^0F_{-2}^{\,1}(\eta,\beta_1)}{{}^0F_0^{\,3/2}(\eta,\beta_1)} \qquad (18)$$

$$n_2 = \frac{1}{3\pi^2}\left(\frac{2m_2^* k_B T}{h^2}\right)^{3/2} {}^0F_0^{\,3/2}(\eta_2,\beta_2) \qquad (19)$$

$$\mu_2 = \frac{2\pi h^4 eC_l}{m_l^*\left(2m_d^* k_B T\right)^{3/2} E_{def}^2} \frac{{}^0F_{-2}^{\,1}(\eta_2,\beta_2)}{{}^0F_0^{\,3/2}(\eta_2,\beta_2)} \qquad (20)$$

$${}^nF_m^{\,k}(\eta,\beta) = \int_0^\infty \left(-\frac{\partial f}{\partial \varepsilon}\right)\varepsilon^n\left(\varepsilon + \alpha\varepsilon^2\right)^k\left[(1+2\alpha\varepsilon)^2 + 2\right]^{m/2} d\varepsilon \qquad (21)$$

Where k_B is Boltzmann's constant; e is the electron charge; C_l ($C_l = \upsilon_l^2 d$) is a parameter determined by the longitudinal speed of sound υ_l and the atomic density d; α is adjustable parameter, and ε is integration energy; ${}^{n}F_{m}^{k}$ is the generalized Fermi function; $\eta = E_f / k_B T$ and $\eta_2 = \eta - \Delta E / k_B T$ are the reduced Fermi level; h is Planck's constant; m_1* is the first band density of states effective mass, taken as 0.47 m_0. The non-parabolicity parameter, β_1, is given by $\beta_1 = k_B T / E_g$, where E_g is the band gap and $\beta_2 = k_B T / (E_g + \Delta E)$, where ΔE is the energy difference between the first and second band maxima, whose value is 0.06 eV. E_{def} is a combination of deformation potentials for multi-valley systems, which describes the carrier scattering strength by acoustic phonons. We assumed a deformation potential scattering by acoustic phonons dominates. We also did the calculation including ionized impurity scattering for the non-parabolic first band. The deformation potential was fit for the first band, using very low carrier concentration results, and then the second band parameters were adjusted. We fixed the effective mass for the light and heavy band and the band offset as a function of temperature. In this work, the number of degenerate valley used was 2 based on the Fermi surface calculations.

2. Figures S1-S13:

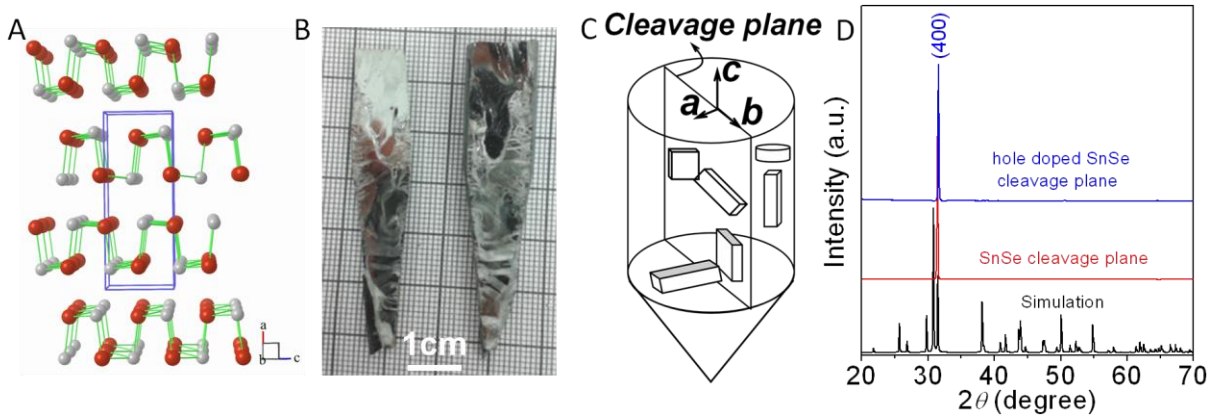

Figures S1. Crystal structure of SnSe, the typical hole doped SnSe crystal, crystal diagram and XRD patterns on the cleavage plane. (**A**) Crystal structure of SnSe along *b* axis, purple, Se atoms; gray, Sn atoms. (**B**) A typical crystal cleaved along the (*l*00) plane. (**C**) The diagram shows how crystals were cut for directional measurements. (**D**) XRD of hole doped SnSe and SnSe (*18*) on the cleavage plane and the SnSe simulation pattern. The (400) reflect plane indicates that SnSe crystal is cleaved at the plane that is perpendicular to *a* axis.

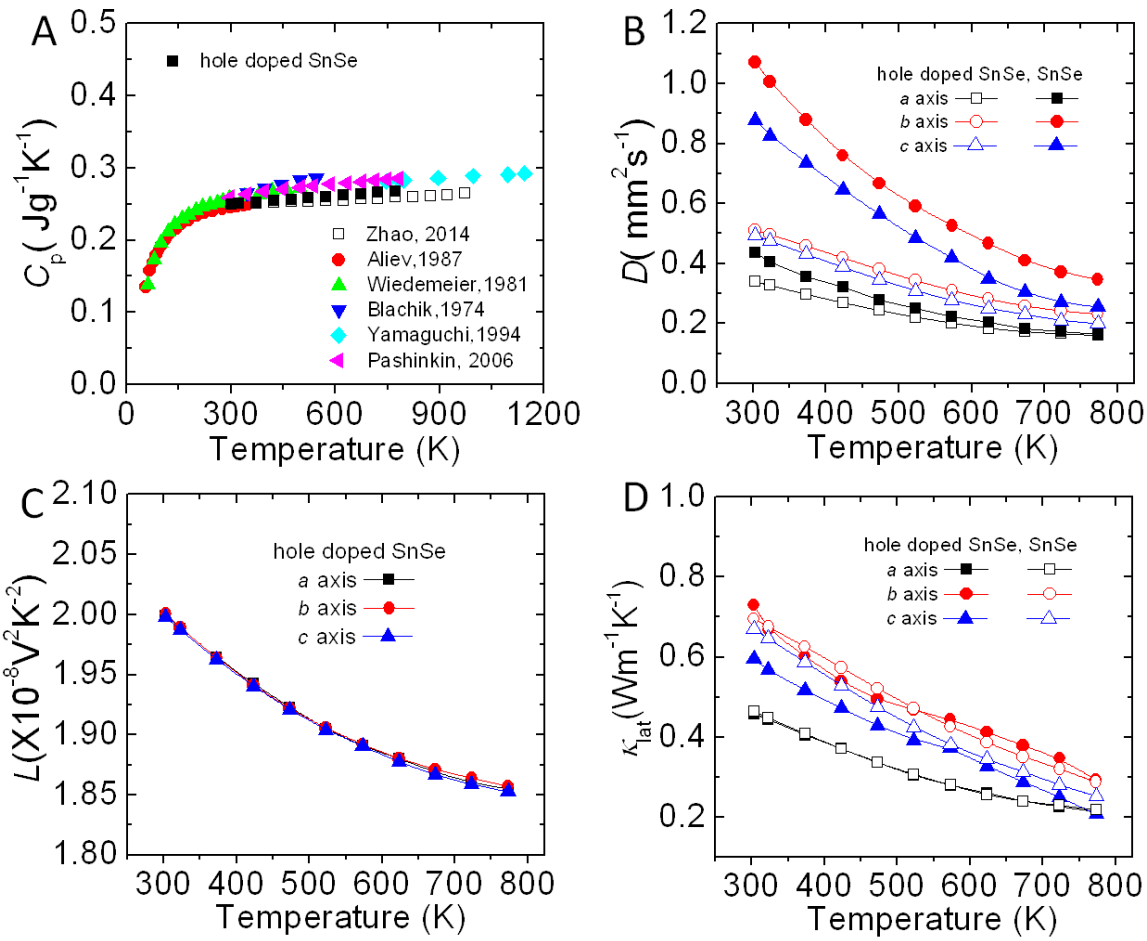

Figures S2. Thermal transport properties of hole doped SnSe crystal. (**A**) Heat capacity comparisons of hole doped SnSe, undoped SnSe (*18*) and other reports for SnSe (*36*). (**B**) Thermal diffusivity comparisons of hole doped SnSe and undoped SnSe (*18*). (**C**) The calculated Lorenz number derived from a multi-band model. (**D**) The lattice thermal conductivity comparisons of hole doped SnSe and undoped SnSe (*18*).

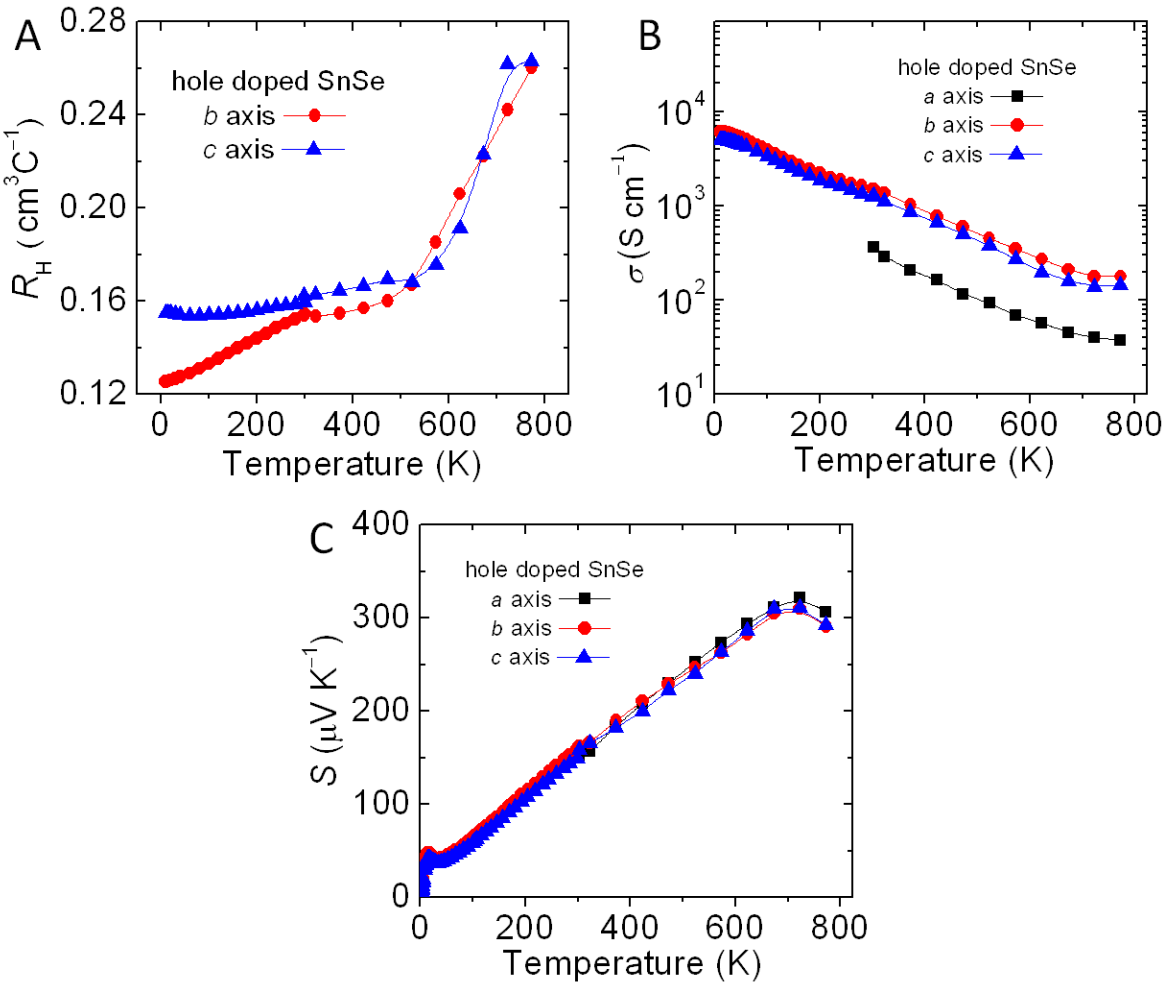

Figures S3. Hall coefficients and electrical transport properties as a function of temperature for hole doped SnSe crystal. (**A**) Hall coefficients. (**B**) Electrical conductivity. (**C**) Seebeck coefficient.

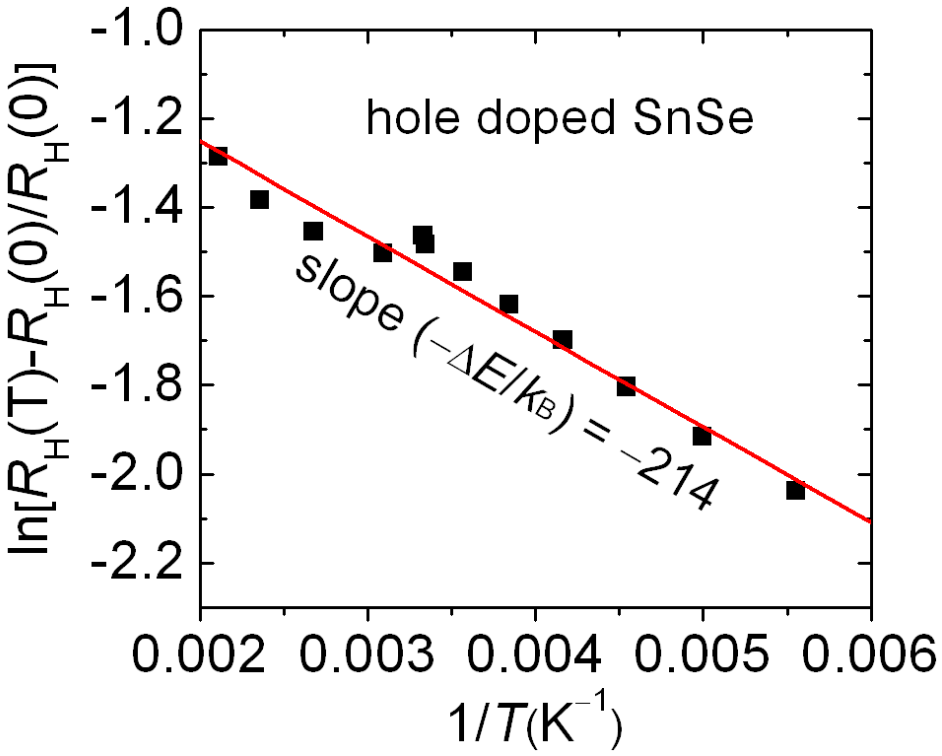

Figures S4. The $\ln[R_H(T)-R_H(0)]/R_H(0)$ as a function of $1/T$ for hole doped SnSe crystals. $\ln[R_H(T)-R_H(0)]/R_H(0)$ as a function of $1/T$ with the solid lines by best linearly fitting the data, the slope ($-\Delta E/k_B$) of -214 yields the energy gap between the first two valence bands, $\Delta E \sim 0.02$ eV.

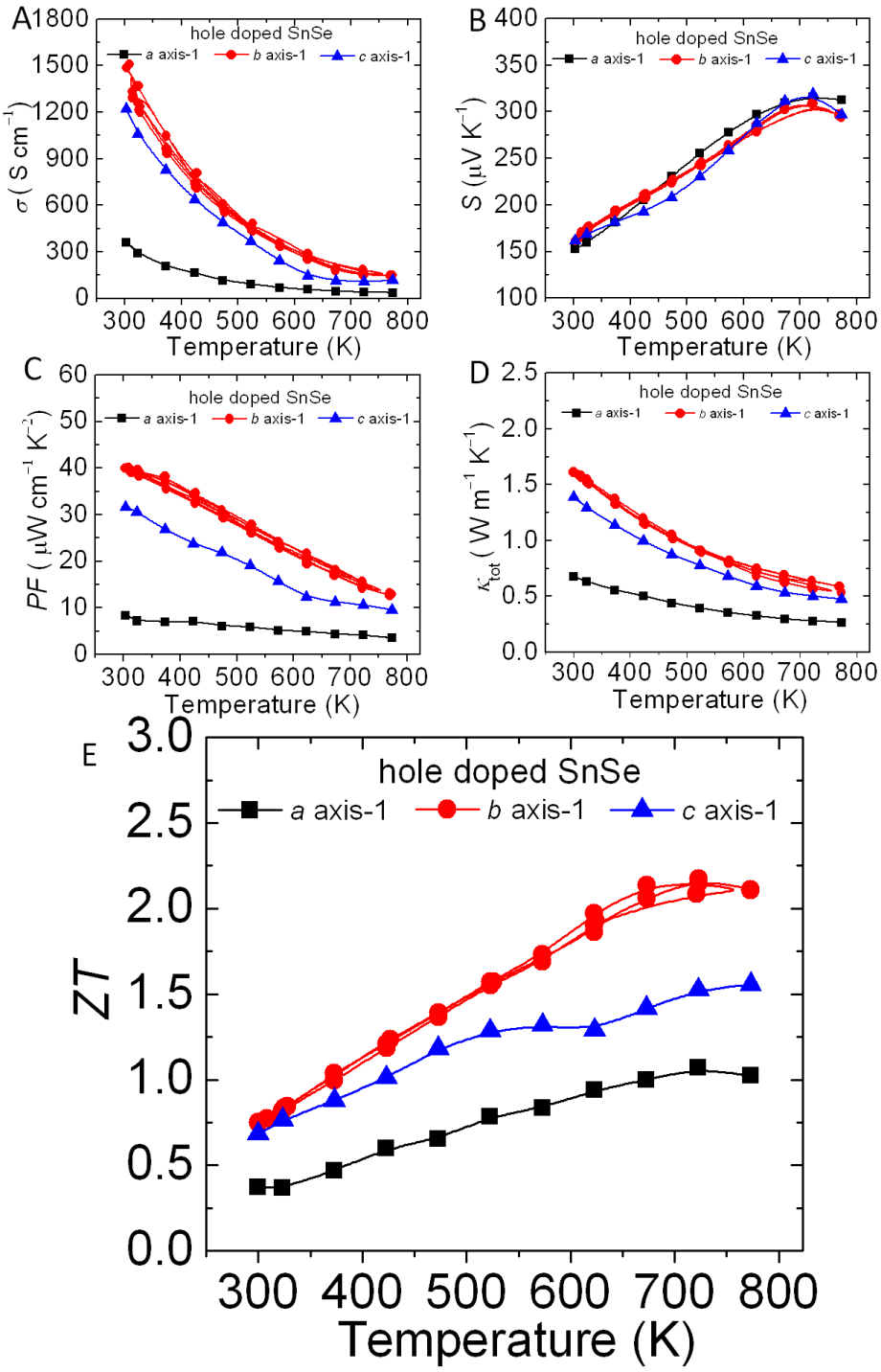

Figures S5. The reproducibility of thermoelectric properties as a function of temperature of hole doped SnSe crystals. (**A**) Electrical conductivity. (**B**) Seebeck coefficient. (**C**) Power factor. (**D**) Total thermal conductivity. (**E**) Figure of merit *ZT*.

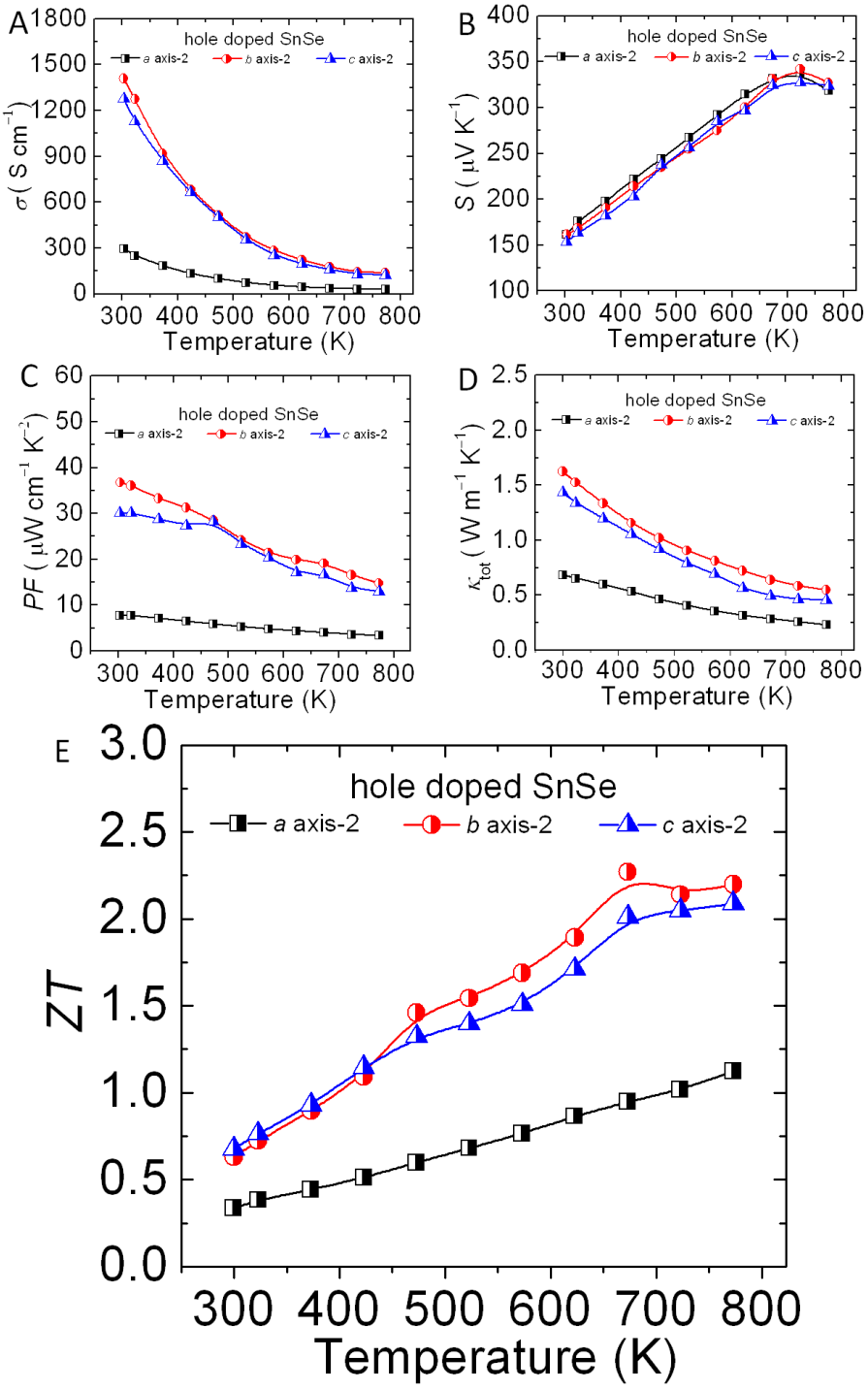

Figures S6. The reproducibility of thermoelectric properties as a function of temperature of hole doped SnSe crystals. (**A**) Electrical conductivity. (**B**) Seebeck coefficient. (**C**) Power factor. (**D**) Total thermal conductivity. (**E**) Figure of merit *ZT*.

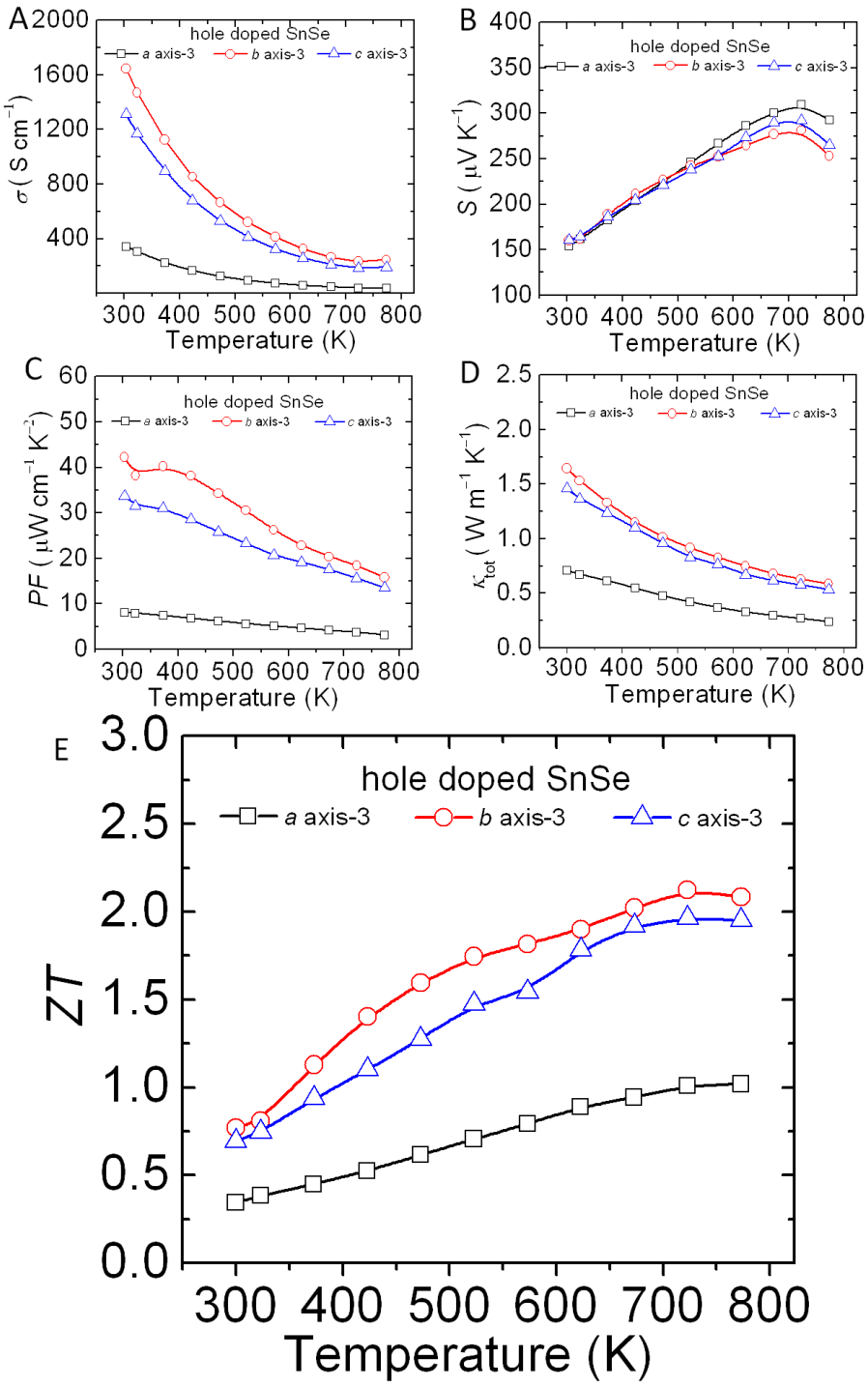

Figures S7. The reproducibility of thermoelectric properties as a function of temperature of hole doped SnSe crystals. (**A**) Electrical conductivity. (**B**) Seebeck coefficient. (**C**) Power factor. (**D**) Total thermal conductivity. (**E**) Figure of merit *ZT*.

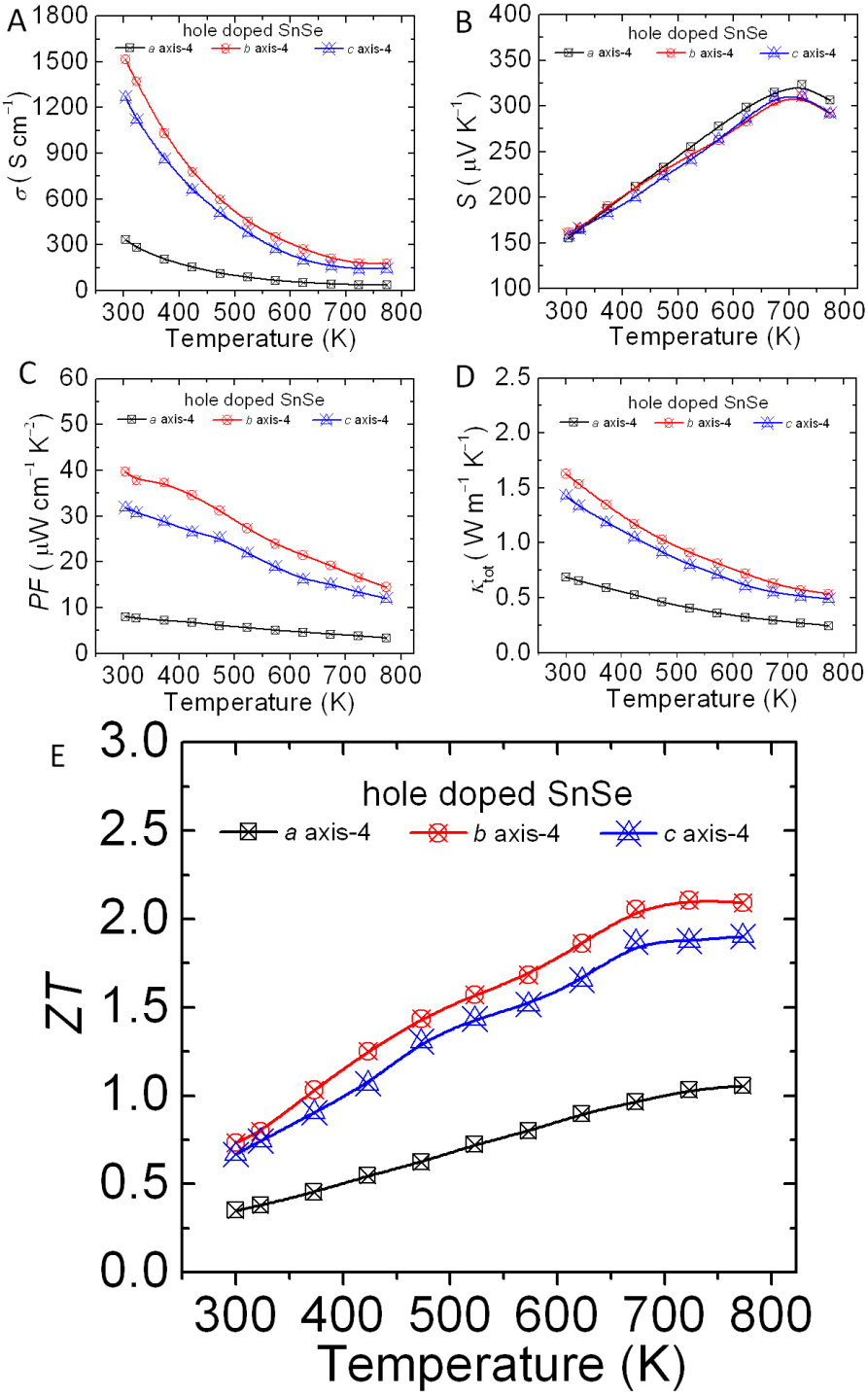

Figures S8. The reproducibility of thermoelectric properties as a function of temperature of hole doped SnSe crystals. (**A**) Electrical conductivity. (**B**) Seebeck coefficient. (**C**) Power factor. (**D**) Total thermal conductivity. (**E**) Figure of merit *ZT*.

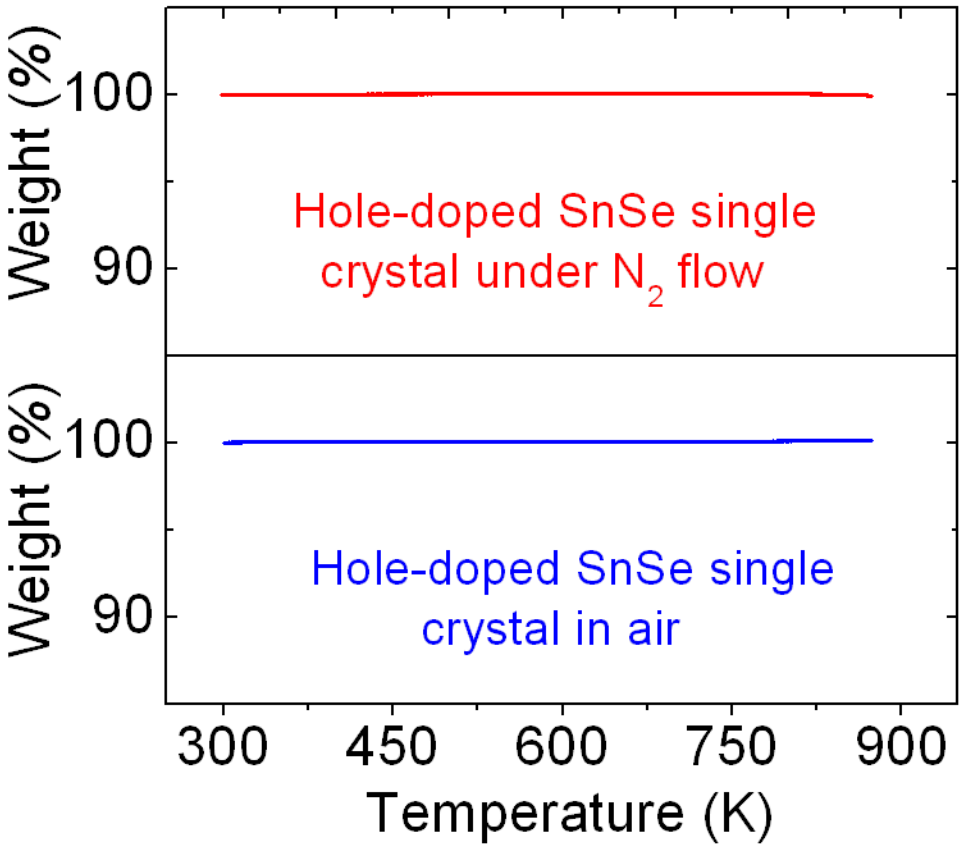

Figures S9. The thermogravimetric analysis (TGA) measurements of hole doped SnSe crystals under N_2 flow (top) and air (bottom).

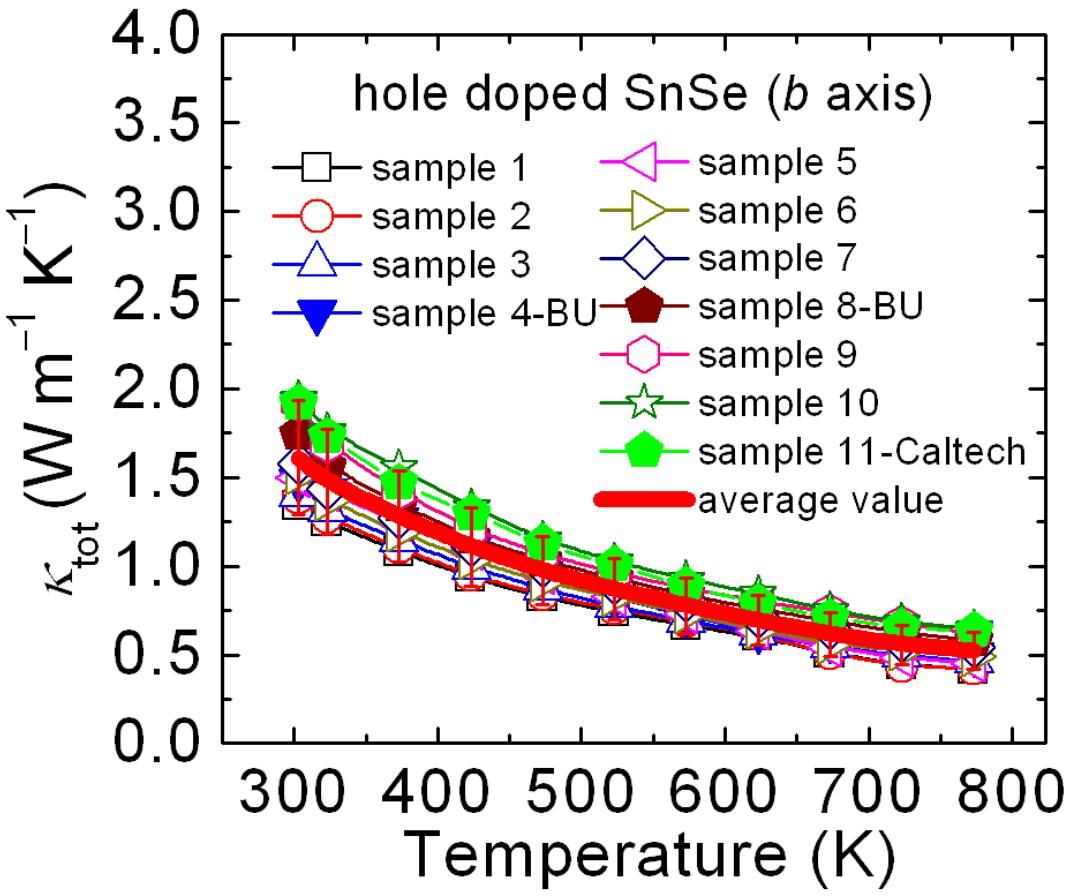

Figures S10. The reproducibility of total thermal conductivities as a function of temperature of hole doped SnSe crystals along *b* axis. BU represents the results measured at Beihang University of China. Caltech represents the results measured at California Institute of Technology of USA. The solid line represents the average value; the measurement uncertainty is about 20 %.

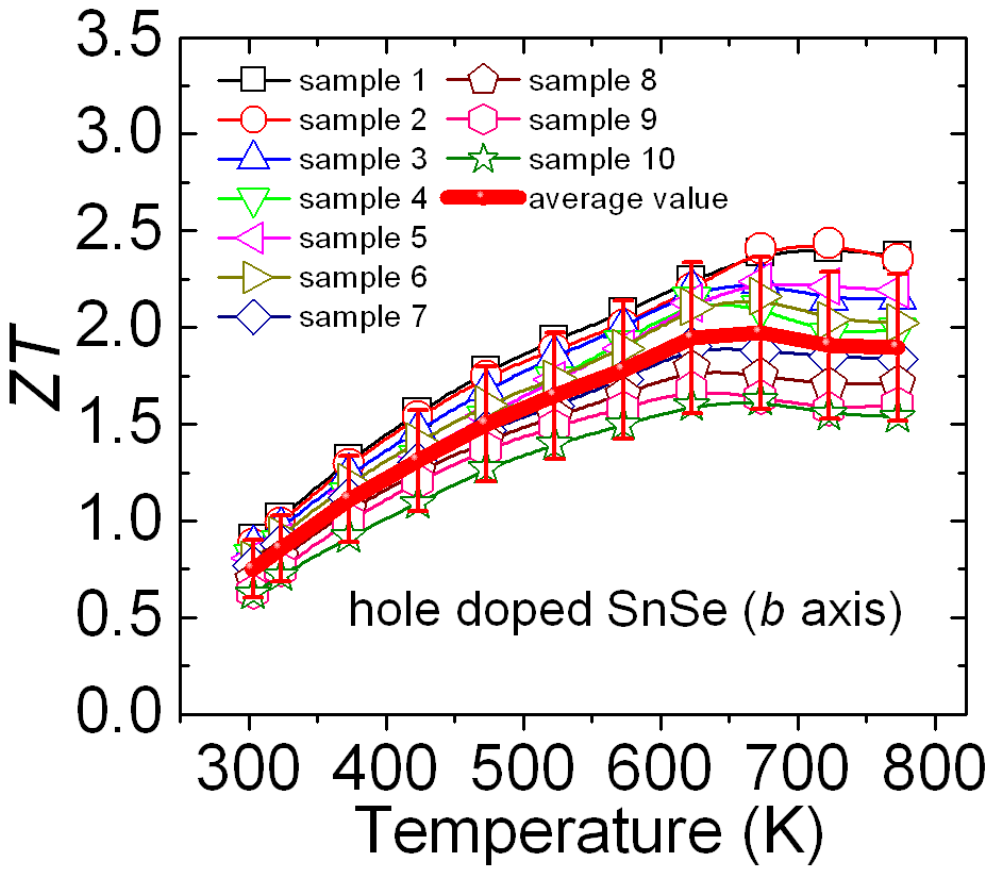

Figures S11. The reproducibility of figure of merit *ZT* as a function of temperature of hole doped SnSe crystals along *b* axis. The solid line represents the average value, the *ZT* measurement uncertainty is about 20 %.

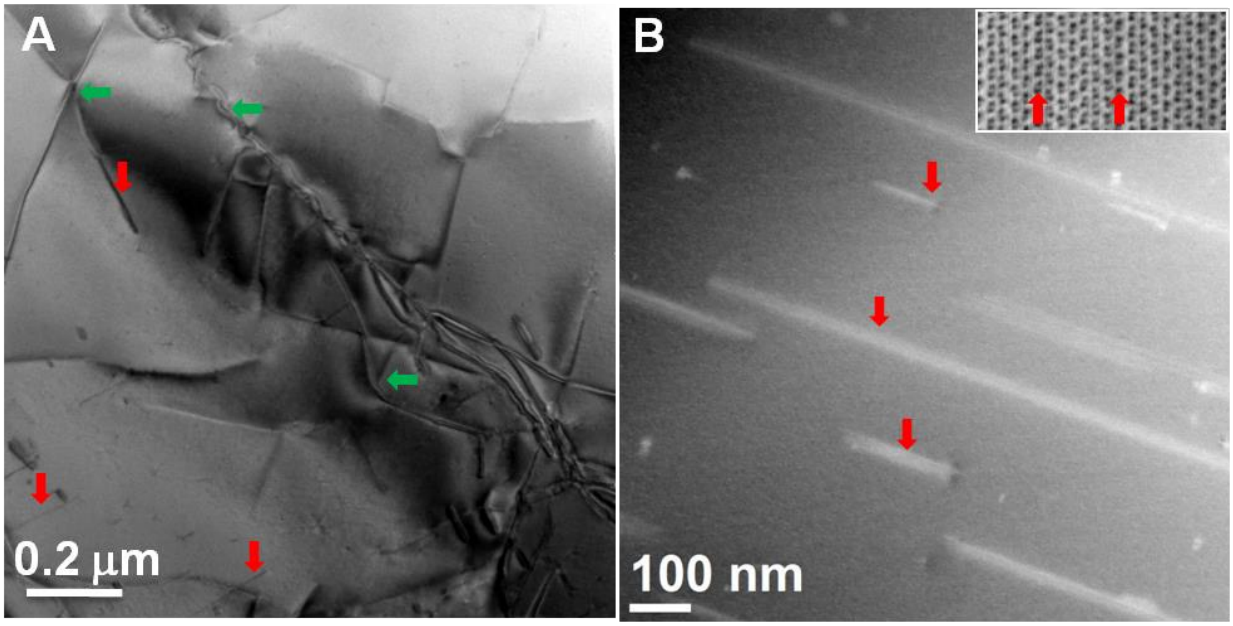

Figures S12. Low-magnification image of the typical regions of the hole doped SnSe in (**A**) TEM model and (**B**) STEM model. The TEM image reveals frequent notable contrast of stacking faults (red vertical arrows) and full/partial edge dislocations (green horizontal arrows). (**B**) The STEM image also shows notable strain contrast of frequent stacking faults (red vertical arrows) in different region of hole doped SnSe sample; inset, the high magnification ABF image indicating the two stacking faults.

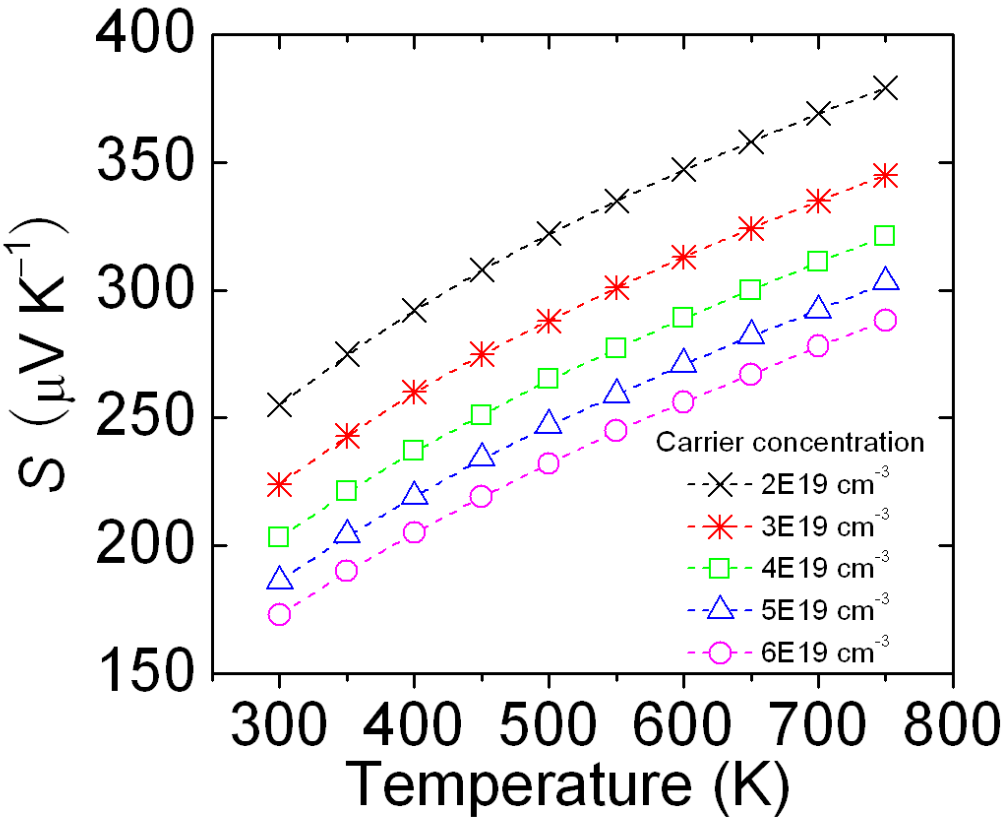

Figures S13. The DFT calculated Seebeck coefficients of SnSe as a function of temperature and doped hole concentration.

3. Additional author notes

Author contributions

L.D.Z. synthesized the samples, designed, carried out thermoelectric experiments and wrote the paper. G.J.T. repeated the samples synthesis and experimental results. S.Q.H. and C.W. carried out the DFT calculations. H.C. and C.U. carried out the Hall measurements and the electrical transport properties at low temperature. Y.L.P., S.K.G., H.B.X., H.W. and G.J.S reconfirmed the thermal transport properties. J.H and V.P.D conducted microscopy experiments, L.D.Z., G.J.T., S.Q.H., J.H., Y.L.P, H.C., H.W., S.K.G., H.B.X., V.P.D., C.U., G.J.S, C.W. and M.G.K. conceived the experiments, analyzed the results and co-edited the manuscript.

4. References

1. L. E. Bell, Cooling, heating, generating power, and recovering waste heat with thermoelectric systems. *Science* **321**, 1457–1461 (2008). Medline

2. J. P. Heremans, M. S. Dresselhaus, L. E. Bell, D. T. Morelli, When thermoelectrics reached the nanoscale. *Nat. Nanotechnol.* **8**, 471–473 (2013). Medline doi:10.1038/nnano.2013.129

3. X. Zhang, L. D. Zhao, Thermoelectric materials: Energy conversion between heat and electricity. *J. Materiomics* **1**, 92–105 (2015). doi:10.1016/j.jmat.2015.01.001

4. M. S. Dresselhaus, G. Chen, M. Y. Tang, R. G. Yang, H. Lee, D. Z. Wang, Z. F. Ren, J. P. Fleurial, P. Gogna, New directions for low-dimensional thermoelectric materials. *Adv. Mater.* **19**, 1043–1053 (2007). doi:10.1002/adma.200600527

5. L. D. Zhao, V. P. Dravid, M. G. Kanatzidis, The panoscopic approach to high performance thermoelectric. *Energy Environ. Sci.* **7**, 251–268 (2014). doi:10.1039/C3EE43099E

6. K. F. Hsu, S. Loo, F. Guo, W. Chen, J. S. Dyck, C. Uher, T. Hogan, E. K. Polychroniadis, M. G. Kanatzidis, Cubic $AgPb_mSbTe_{2+m}$: Bulk thermoelectric materials with high figure of merit. *Science* **303**, 818–821 (2004). Medline doi:10.1126/science.1092963

7. B. Poudel, Q. Hao, Y. Ma, Y. Lan, A. Minnich, B. Yu, X. Yan, D. Wang, A. Muto, D. Vashaee, X. Chen, J. Liu, M. S. Dresselhaus, G. Chen, Z. Ren, High-thermoelectric performance of nanostructured bismuth antimony telluride bulk alloys. *Science* **320**, 634–638 (2008). Medline doi:10.1126/science.1156446

8. M. Zhou, J. F. Li, T. Kita, Nanostructured $AgPb_mSbTe_{m+2}$ system bulk materials with enhanced thermoelectric performance. *J. Am. Chem. Soc.* **130**, 4527–4532 (2008). Medline doi:10.1021/ja7110652

9. K. Biswas, J. He, I. D. Blum, C. I. Wu, T. P. Hogan, D. N. Seidman, V. P. Dravid, M. G. Kanatzidis, High-performance bulk thermoelectrics with all-scale hierarchical architectures. *Nature* **489**, 414–418 (2012). Medline doi:10.1038/nature11439

10. P. F. R. Poudeu, J. D'Angelo, A. D. Downey, J. L. Short, T. P. Hogan, M. G. Kanatzidis, High thermoelectric figure of merit and nanostructuring in bulk p-type $Na_{1-x}Pb_mSb_yTe_{m+2}$. *Angew. Chem. Int. Ed.* **45**, 3835–3839 (2006). Medline doi:10.1002/anie.200600865

11. J. P. Heremans, V. Jovovic, E. S. Toberer, A. Saramat, K. Kurosaki, A. Charoenphakdee, S. Yamanaka, G. J. Snyder, Enhancement of thermoelectric efficiency in PbTe by distortion of the electronic density of states. *Science* **321**, 554–557 (2008). Medline

12. Y. Pei, X. Shi, A. LaLonde, H. Wang, L. Chen, G. J. Snyder, Convergence of electronic bands for high performance bulk thermoelectrics. *Nature* **473**, 66–69 (2011). Medline doi:10.1038/nature09996

13. W. Liu, X. Tan, K. Yin, H. Liu, X. Tang, J. Shi, Q. Zhang, C. Uher, Convergence of conduction bands as a means of enhancing thermoelectric performance of n-type $Mg_2Si_{(1-x)}Sn_{(x)}$ solid solutions. *Phys. Rev. Lett.* **108**, 166601 (2012). Medline doi:10.1103/PhysRevLett.108.166601

14. H. Z. Zhao, J. H. Sui, Z. J. Tang, Y. C. Lan, Q. G. Jie, D. Kraemer, K. N. McEnaney, A. Guloy, G. Chen, Z. F. Ren, High thermoelectric performance of MgAgSb-based materials. *Nano Energy* **7**, 97–103 (2014). doi:10.1016/j.nanoen.2014.04.012

15. L. D. Zhao, S. Hao, S. H. Lo, C. I. Wu, X. Zhou, Y. Lee, H. Li, K. Biswas, T. P. Hogan, C. Uher, C. Wolverton, V. P. Dravid, M. G. Kanatzidis, High thermoelectric performance via hierarchical compositionally alloyed nanostructures. *J. Am. Chem. Soc.* **135**, 7364–7370 (2013). Medline doi:10.1021/ja403134b

16. X. Shi, J. Yang, J. R. Salvador, M. Chi, J. Y. Cho, H. Wang, S. Bai, J. Yang, W. Zhang, L. Chen, Multiple-filled skutterudites: High thermoelectric figure of merit through separately optimizing electrical and thermal transports. *J. Am. Chem. Soc.* **133**, 7837–7846 (2011). Medline doi:10.1021/ja111199y

17. M. M. Nassary, The electrical conduction mechanisms and thermoelectric power of SnSe single crystals. *Turk. J. Phys.* **33**, 201–208 (2009). doi:10.3906/fiz-0811-9

18. L. D. Zhao, S. H. Lo, Y. Zhang, H. Sun, G. Tan, C. Uher, C. Wolverton, V. P. Dravid, M. G. Kanatzidis, Ultralow thermal conductivity and high thermoelectric figure of merit in SnSe crystals. *Nature* **508**, 373–377 (2014). Medline doi:10.1038/nature13184

19. Y. I. Ravich, B. A. Efimova, I. A. Smirnov, *Semiconducting Lead Chalcogenides.* (Plenum press, 1970), vol. 5.

20. S. I. Kim, K. H. Lee, H. A. Mun, H. S. Kim, S. W. Hwang, J. W. Roh, D. J. Yang, W. H. Shin, X. S. Li, Y. H. Lee, G. J. Snyder, S. W. Kim, Dense dislocation arrays embedded in grain boundaries for high-performance bulk thermoelectrics. *Science* **348**, 109–114 (2015). Medline doi:10.1126/science.aaa4166

21. S. K. Placheova, Thermoelectric figure of merit of the system $(GeTe)_{1-x}(AgSbTe_2)_x$. *Phys. Status Solidi* **83**, 349–355 (1984) (a). doi:10.1002/pssa.2210830140

22. G. J. Snyder, in *Thermoelectrics Handbook: Macro to Nano*, D. M. Rowe, Ed. (CRC Press, 2006), chap. 9.

23. H. J. Wu, L. D. Zhao, F. S. Zheng, D. Wu, Y. L. Pei, X. Tong, M. G. Kanatzidis, J. Q. He, Broad temperature plateau for thermoelectric figure of merit *ZT*>2 in phase-separated $PbTe_{0.7}S_{0.3}$. *Nat. Commun.* **5**, 4515 (2014). Medline

24. D. M. Rowe, *CRC Handbook of Thermoelectrics* (CRC Press, London, 1995).

25. C. W. Li, J. Hong, A. F. May, D. Bansal, S. Chi, T. Hong, G. Ehlers, O. Delaire, Orbitally driven giant phonon anharmonicity in SnSe. *Nat. Phys.* 10.1038/NPHYS3492 (2015). 10.1038/NPHYS3492

26. F. Serrano-Sánchez, M. Gharsallah, N. M. Nemes, F. J. Mompean, J. L. Martinez, J. A. Alonso, Record Seebeck coefficient and extremely low thermal conductivity in nanostructured SnSe. *Appl. Phys. Lett.* **106**, 083902 (2015). doi:10.1063/1.4913260

27. Q. Zhang, E. K. Chere, J. Sun, F. Cao, K. Dahal, S. Chen, G. Chen, Z. Ren, Studies on thermoelectric properties of n-type polycrystalline $SnSe_{1-x}S_x$ by iodine doping. *Adv. Energy Mater.* **5**, 1500360 (2015). doi:10.1002/aenm.201500360

28. H. Wang, Y. Pei, A. D. LaLonde, G. J. Snyder, Heavily doped p-type PbSe with high thermoelectric performance: An alternative for PbTe. *Adv. Mater.* **23**, 1366–1370 (2011). Medline doi:10.1002/adma.201004200

29. L. D. Zhao, J. He, C. I. Wu, T. P. Hogan, X. Zhou, C. Uher, V. P. Dravid, M. G. Kanatzidis, Thermoelectrics with earth abundant elements: High performance p-type PbS nanostructured with SrS and CaS. *J. Am. Chem. Soc.* **134**, 7902–7912 (2012). Medline doi:10.1021/ja301772w

30. G. Tan, L. D. Zhao, F. Shi, J. W. Doak, S.-H. Lo, H. Sun, C. Wolverton, V. P. Dravid, C. Uher, M. G. Kanatzidis, High thermoelectric performance of p-type SnTe via a synergistic band engineering and nanostructuring approach. *J. Am. Chem. Soc.* **136**, 7006–7017 (2014). Medline doi:10.1021/ja500860m

31. Y. Pei, H. Wang, G. J. Snyder, Band engineering of thermoelectric materials. *Adv. Mater.* **24**, 6125–6135 (2012). Medline doi:10.1002/adma.201202919

32. G. Shi, E. Kioupakis, Quasiparticle band structures and thermoelectric transport properties of p-type SnSe. *J. Appl. Phys.* **117**, 065103 (2015). doi:10.1063/1.4907805

33. Calculation details are available as supplementary materials on *Science* Online.

34. C. L. Chen, H. Wang, Y. Y. Chen, T. Day, G. J. Snyder, Thermoelectric properties of p-type polycrystalline SnSe doped with Ag. *J. Mater. Chem. A* **2**, 11171–11176 (2014). doi:10.1039/c4ta01643b

35. S. Sassi, C. Candolfi, J. B. Vaney, V. Ohorodniichuk, P. Masschelein, A. Dauscher, B. Lenoir, Assessment of the thermoelectric performance of polycrystalline p-type SnSe. *Appl. Phys. Lett.* **104**, 212105 (2014). doi:10.1063/1.4880817

36. A. S. Pashinkin, A. S. Malkova, V. A. Fedorov, M. S. Mikhailova, Heat capacity of tin monoselenide. *Inorg. Mater.* **42**, 593–595 (2006). doi:10.1134/S0020168506060033

37. A. Agarwal, S. H. Chaki, D. Lakshminarayana, Growth and thermal studies of SnSe single crystals. *Mater. Lett.* **61**, 5188–5190 (2007). doi:10.1016/j.matlet.2007.04.026

38. P. E. Blöchl, Projector augmented-wave method. *Phys. Rev. B Condens. Matter Mater. Phys.* **50**, 17953–17979 (1994). Medline doi:10.1103/PhysRevB.50.17953

39. J. P. Perdew, K. Burke, M. Ernzerhof, Generalized gradient approximation made simple. *Phys. Rev. Lett.* **77**, 3865–3868 (1996). Medline doi:10.1103/PhysRevLett.77.3865

40. G. Kresse, J. Furthmüller, Efficient iterative schemes for ab initio total-energy calculations using a plane-wave basis set. *Phys. Rev. B Condens. Matter Mater. Phys.* **54**, 11169–11186 (1996). Medline doi:10.1103/PhysRevB.54.11169

41. H. J. Goldsmid, *Thermoelectric Refrigeration*. (Plenum Press, 1964), p. 58.

42. M. S. Dresselhaus, Y.-M. Lin, S. B. Cronin, O. Rabin, M. R. Black, G. Dresselhaus, *Quantum wells and quantum wires for potential thermoelectric applications*, in *Recent Trends in Thermoelectric Materials Research III*, Editor: T. M. Tritt, (Academic Press, 2001), p.1-121.

43. G. K. H. Madsen, D. J. Singh, BoltzTraP. A code for calculating band-structure dependent quantities. *Comput. Phys. Commun.* **175**, 67–71 (2006). doi:10.1016/j.cpc.2006.03.007

44. N. V. Kolomoet, M. N. Vinograd, L. M. Sysoeva, Valence band of PbTe. *Sov. Phys. Semicond. -USSR* **1**, 1020 (1968).

45. J. P. Heremans, B. Wiendlocha, A. M. Chamoire, Resonant levels in bulk thermoelectric semiconductors. *Energy Environ Sci.* **5**, 5510–5530 (2012). doi:10.1039/C1EE02612G

46. Q. Zhang, F. Cao, W. Liu, K. Lukas, B. Yu, S. Chen, C. Opeil, D. Broido, G. Chen, Z. Ren, Heavy doping and band engineering by potassium to improve the thermoelectric figure of merit in p-type PbTe, PbSe, and $PbTe_{1-y}Se_y$. *J. Am. Chem. Soc.* **134**, 10031–10038 (2012). Medline doi:10.1021/ja301245b

47. H. Wang, J.-H. Bahk, C. Kang, J. Hwang, K. Kim, J. Kim, P. Burke, J. E. Bowers, A. C. Gossard, A. Shakouri, W. Kim, Right sizes of nano- and microstructures for high-performance and rigid bulk thermoelectrics. *Proc. Natl. Acad. Sci. U.S.A.* **111**, 10949–10954 (2014). Medline doi:10.1073/pnas.1403601111